Journal of Ultrafine Grained and Nanostructured Materials
https://jufgnsm.ut.ac.ir
Vol. 57, No.2, December 2024, pp. 236-256
Print ISSN: 2423-6845 Online ISSN: 2423-6837
DOI: 10.22059/jufgnsm.2024.02.12

An in-silico investigation of biomechanical response of cardiovascular stents during deployment inside a stenotic artery

Milad Rajabi[1], Ali Reza Eivani[*,1], Seyed Hossein Seyedein[1], Jie Zhou[2]*

[1]School of Metallurgy and Materials Engineering, Iran University of Science and Technology, Tehran, Iran;

[2]Department of Biomechanical Engineering, Delft University of Technology, Mekelweg 2, 2628 CD Delft, the Netherlands.

Recieved: 18 June 2024; Accepted: 20 November 2024

**Corresponding author email: aeivani@iust.ac.ir*

ABSTRACT

Three commercial stents (Palmaz-Schatz, NIR, and BioMatrix) with either an open-cell (20% open-cell) or a closed-cell (80% closed-cell) design, and one new hybrid stent design were numerically modeled using the ABAQUS/Explicit finite element software (Dassault Systèmes, France) to compare their behaviors during deployment in a stenotic artery. The ABAQUS/Explicit dynamic explicit solver was utilized to efficiently capture the complex interactions between the balloon, stent, artery, and plaque during the stent expansion process. The effect of changing the material from stainless steel (SS 316L) to cobalt-chromium (CoCr) and platinum-chromium (PtCr), as well as the reduced thickness of struts from 0.1 mm to 0.08 mm, were investigated. The new hybrid stent design featured reduced axial strut spacing (from 1.2 mm to 0.8 mm), larger corner radii (from 0.2 mm to 0.3 mm), and smaller amplitudes in the ring (from 1.0 mm to 0.8 mm). For the simulations, a balloon-stent-artery model with plaque and average blood pressure of 80 mmHg was used. The results showed that the new hybrid stent did not perform worse in any of the studied biomechanical parameters compared to the commercial open-cell (20% expansion) and closed-cell (15% expansion) stents, and exhibited better performance in maximum expansion (22%) and recoil responses (5% recoil). Changing the material in the new hybrid stent from SS 316L to CoCr or PtCr improved the biomechanical behavior, such as expansion (25%), recoil (3%), and dogboning (0.9), but increased the maximum von Mises stress on the artery-plaque system by 18%. Reducing the strut thickness from 0.1 mm to 0.08 mm decreased the maximum stress on the artery-plaque system by 12%, but undesirably increased dogboning (1.1) and recoil (7%).

Keywords: *Finite element method; Stent deployment; Geometry; Material; Stenotic artery.*

1. Introduction

Biomedical research including material design and development, coating and surface processing and modelling and computational activities play a crucial role in advancing medical technologies and improving patient outcomes [1-5]. Cardiovascular disease is one of the leading causes of death in the world, so that according to the study Global Burden of Disease (GBD) in 2015, cardiovascular disease caused the death of 17.9 million people in the world, which accounts for 31% of the total deaths [6]. It is also predicted that by 2030, 23.6 million people will die annually due to cardiovascular disease [7], which is why studies in this field are of great importance. One of the main causes of cardiovascular disease is atherosclerosis [8] and one of the simplest and most effective methods of treating this disease is the use of stents [9]. Today, there are various commercially available stents in terms of geometry and materials. In terms of design pattern, these stents can be classified into a closed-cell, or an open-cell, or a hybrid designs [10].

The most commonly used metal materials used in coronary stents are 316L stainless steel, cobalt-chromium alloys, tantalum, nitinol, titanium alloys and platinum alloys [11-16]. To make an appropriate choice among the available stents, one needs to understand the biomechanical behavior in addition to the physio-biological performance. To evaluate stents with this variety in geometry and materials, are used in-vitro, in-vivo and clinical tests are used. Although the use of these tests is very efficient and is required to obtain food and drug approval, it requires a lot of time, money and equipment. Also in clinical tests, the anatomy and pathology of coronary heart disease may vary from person to person and affect the results. In-silico tests help to evaluate stents in terms of geometry and material under the same conditions. In-silico tests performed using Finite Element Methods (FEM) have been used to simulate different components in stent implants and to achieve faster, more efficient and cost-effective results [17, 18].

The first the Final Element Simulations (FES) were very simple to model the behavior of the stent in fact, and only the stent was modeled in simulation, and by applying pressure to the inside of the stent, expansion of the stent was simulated, that was certainly not the correct simulation for stent expansion as they did not consider other components such as balloon, artery, plaque and blood pressure. the first simulations in this field are the study of Dumoulin and Cochelin [19], Migliavacca et al. [20] and Chua et al. [21]. In later years, in studies of Chua et al. [22], Chua et al. [23], Wang et al. [24], Xia et al. [25], Ju et al. [26], Lim et al. [27], Park et al. [28] and Kumar et al. [29] studies, balloon-stent models were used to simulate stent expansion. In this model, pressure is not applied directly to the inner surface of the stent, but first applied to the inner surface of the balloon and then, transmitted to the stent through the contact between the balloon and the stent. In other studies, stent-artery model without plaque [30] and stent-artery with plaque and average blood pressure [31] were used. In these studies, a balloon and artery were modeled as a linear elastic material. Zhao et al. [32] also used the stent-artery model, without plaque and without applying average blood pressure, to study balloon-expanding stents with stainless steel 316L, cobalt-chrome alloy, and self-expanding stents with nitinol material. In addition, in examining the effect of material, the stents did not have the same geometry and this geometry difference affects the results and it causes a correct comparison to investigation the effect of the material. In 2017, Conway et al [17]. To examine cobalt-chromium, stainless steel 316L and platinum chrome stents used the stent-artery model without plaque and applying average blood pressure. The stent-artery model with plaque and average blood pressure was used in other studies in which the behavior of the artery and plaque was modeled hyperelastic [33, 34]. In 2009, Zahedmanesh et al. [35] used the stent-artery model, in which artery had three layers of intima, media, and adventitia with plaque and was simulated with third order Ogden hyperelastic equation. Schiavone et al. [36] also used balloon-stent-artery model, with plaque and without average blood pressure, to evaluate cobalt-chromium stent and stainless steel 316L. The model presented in this study was relatively complete, but the study of the material was not performed in the same design so that only the effect of the material is involved in the results. The most complete presented model was the balloon-stent-artery model with plaque, which was introduced in the following years [37-42]. In these studies, either blood pressure was not considered or the artery was not modeled as three layers of intima, media and adventitia.

Across the previously published articles in this field, due to the reduction of computational complexity and the reduction of FES solution time, the effects of such parameters as tissue-stent interaction, balloon, plaque and blood pressure have been partially or completely neglected, or considered in a simplified way, although these parameters are of great importance, as they can affect the biomechanical behavior of stent during deployment to a great extent. In the present research, in order to investigate the effect of design, material and thickness of struts on mechanical behaviors of stents with new hybrid design, the balloon-stent-artery model with plaque and average blood pressure was used. The artery was modeled as three layers of intima, media, and adventitia. Also, the behavior of plaque and artery was modeled hyperelastic. All of these factors were chosen, combined and implemented in modeling so as to bring the FES close to the real situation and to advance the state of the art. In addition, a new hybrid stent design compared with the three commercial stents with open-cell and closed-cell designs was proposed and mechanical behavior is investigated. The comprehensive finite

element modeling approach employed in this study provides valuable insights into the detailed biomechanical response of various stent designs during deployment within a stenotic artery. The use of the ABAQUS/Explicit software with its dynamic explicit solver allowed the researchers to efficiently capture the complex interactions between the balloon, stent, artery, and plaque, which is crucial for accurately simulating the stent deployment process. Incorporating realistic modeling of the artery layers (intima, media, and adventitia), plaque behavior, and average blood pressure conditions further enhances the validity of the results compared to simplified models. However, the study is limited to numerical simulations, and experimental validation of the stent performance would be necessary to fully confirm the findings. Additionally, while the new hybrid stent design shows promising results, its long-term clinical performance in terms of preventing restenosis and ensuring vessel patency would need to be evaluated through in-vivo studies or clinical trials. Nevertheless, the comprehensive in-silico approach demonstrated in this work provides a robust framework for evaluating stent designs and materials prior to physical prototyping and testing.

2. FE simulation

The finite element simulations were performed using the ABAQUS/Explicit software package (Dassault Systèmes, France). ABAQUS/Explicit was chosen as the computational platform due to its capability in handling large deformations and nonlinear material behaviors associated with the stent deployment process. The dynamic explicit solver was utilized to efficiently capture the complex interactions between the balloon, stent, artery, and plaque during the stent expansion. This comprehensive finite element modeling approach, incorporating the ABAQUS/Explicit software, allowed the researchers to investigate the detailed biomechanical response of the various stent designs under realistic deployment conditions within the stenotic artery.

2.1. Geometric models

The Palmaz-Schatz, NIR and BioMatrix stents, as well as a proposed hybrid stent, were modelled. According to studies by Bedoya et al. [43], in the design of the new hybrid stent, an attempt was made to reduce the adverse effects of the stent by reducing the axial strut spacing, larger corners and smaller amplitudes in the ring. The new hybrid stent consists of a total of 20 hybrid cell units (one closed cell and one open cell), while there are 5 cell units per stent length and 4 cell units per stent radial axis. The geometric dimensions of each unit cell are shown in Fig. 1. Also, the new stent is divided into two categories based on the thickness of the Struts: stent A and stent B. The geometric parameters and structural features of these stents are listed in Table 1. Geometrical models of the stents with a length of 10 mm (Fig. 2) were created in SolidWorks (Dassault Systèmes). The Palmaz-Schutz and NIR stents had closed-cell designs, while BioMatrix stent had an open-cell design. In order to alleviate the shortcomings of these two designs, two hybrid stent design were proposed. The initial inner diameter, in which a deflated balloon was placed, was 3 mm. The strut thicknesses were 90, 100, 120, 80 and 60 μm for the Palmaz-Schatz, NIR, BioMatrix, stent A and stent B, respectively. The 60-120 μm range was likely chosen based on the researchers' understanding of the current trends and best practices in stent design, aiming to strike a balance between the mechanical properties and clinical outcomes.

The balloon was modeled as a thin-walled hollow cylinder with an outer diameter of 2.9 mm and a wall thickness of 0.1 mm. The length of the rubber balloon was 12 mm so that it protruded from each side of the 10 mm long stent by 1 mm. The artery was modeled as a hollow cylinder. A modeled artery section was 20 mm long and had an inner diameter

Table 1- Geometric parameters and structural features of the stents under investigation

stent	Diameter (mm)	Length (mm)	Strut thickness (μm)	Strut width (μm)	Number of rings	Number of U-bends in each ring	Stent design
Palmaz-Schatz	3	10	90	70	-	-	closed-cell
NIR	3	10	100	100	4	24	closed-cell
BioMatrix	3	10	120	120	5	24	open-cell
new stent A	3	10	80	100	6	24	hybrid
new stent B	3	10	60	100	6	24	hybrid

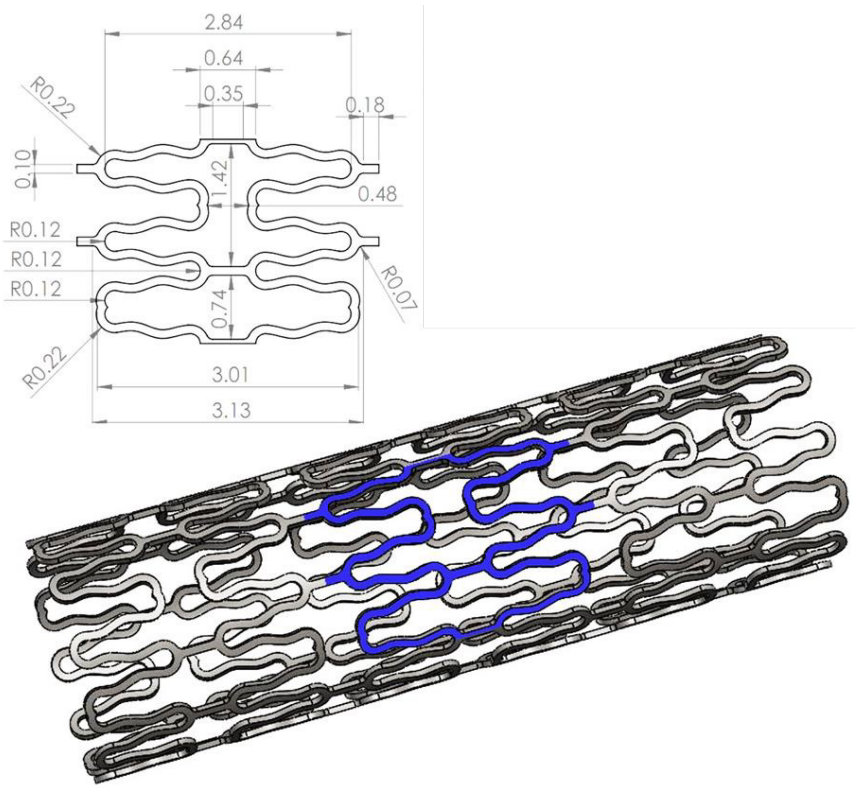

Fig. 1- New hybrid stent and geometric dimensions of each cell unit.

of 4 mm and a total wall thickness of 1 mm. As shown in Fig. 3, the stenotic artery was considered to consist of three tissue layers, i.e., intima, media and adventitia, with thicknesses of 0.27, 0.35 and 0.38 mm, respectively. The plaque deposited on the inner wall of the artery symmetrically and axially.

In most of previous studies, the plaque was modeled as a hollow cylinder with a curved inner wall. The simplified plaque shape decreased the accuracy of the predicted biomechanical behavior of the stent during deployment, considering the fact that the plaque shape can have a significant effect on the performance of the stent. The same stent can behave differently, when implanted into arteries with different plaque shapes. In this research, the Hicks-Henne bump function [44] was used to represent the plaque shape and its effect on the mechanical behavior of the stent. This model was previously used by other researchers, for example, by Kolachalama et.al. [45], to define the plaque shape in the artery. The Hicks-Henne bump function used to create a standard and valid shape for the plaque is expressed by equation below. [44]

$$y = A[sin\ sin\ \left(\pi x^{\left(-\frac{ln2}{lnx_p}\right)}\right)]^t\ ;\ for\ 0 < x < 1$$

Where A is the thickness of the maximum stenosis, x_p is the location of the peak and t indicates the shape of the peak. A large t value corresponds to a sharp peak and by the same token a reduced t value represents a blunt peak. The following function can be used for a plaque with a desired length L and a base thickness of t_b [44].

$$y = t_b + (A - t_b)\left[sin\ sin\ \pi \left(\frac{x}{L}\right)^{\left(-\frac{ln2}{lnx_p}\right)}\right]^t\ ;\ for\ 0 < x < L$$

Fig. 3 shows the plaque shape and the Hicks-Henne bump function when A = 0.5 mm, x_p = 0.5, t = 2, t_b = 0.01 mm and L = 15 mm, representing 43.75% diameter stenosis at the middle section.

2.2 Materials and constitutive models

In order to improve the performance of the new stent, three materials were examined to investigate the effect of the material on the behavior of the stent too. A bilinear elastic-plastic stress-strain relationship was used to define the properties of stainless steel 316L, CoCr alloy (type L605) and PtCr alloy (33% by weight of platinum) that the properties parameters for the three materials are shown in the Table 2 .

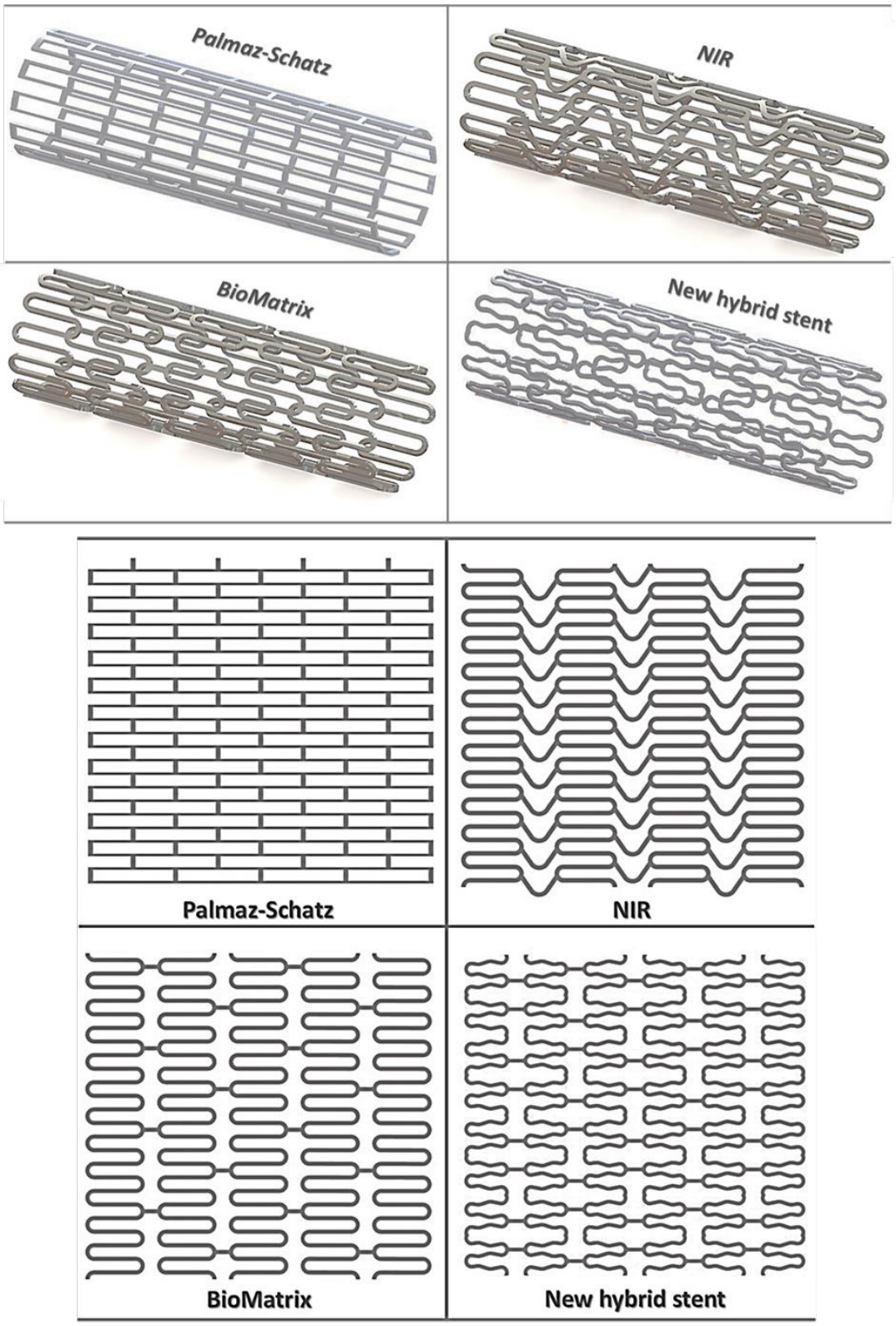

Fig. 2- Three-dimensional and two-dimensional views of the four different stents investigated in this study, names of each stent design are added on top of the images.

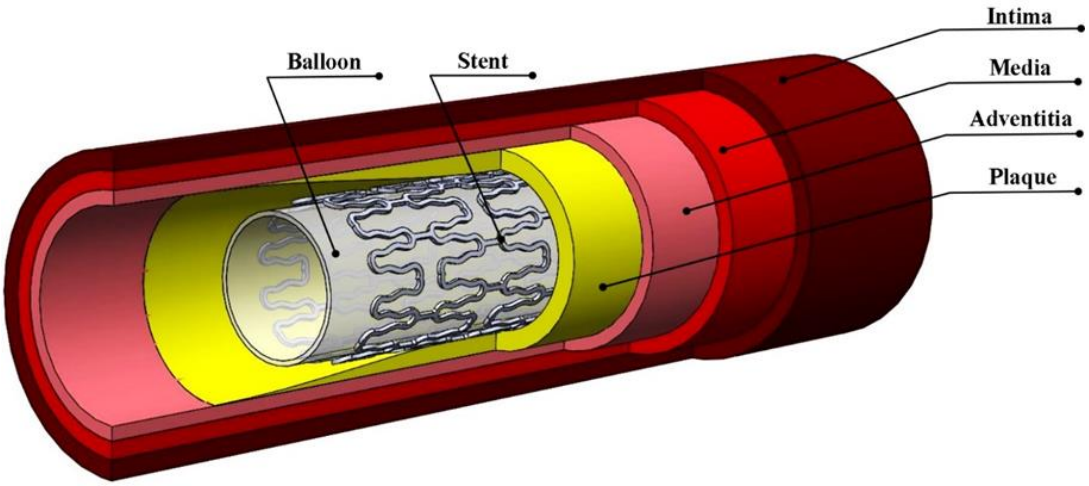

Fig. 3- shows all the components of the simulation and assembly.

Table 2- properties parameters for SS316L, CoCr L605 and PtCr [37, 49]

material	Density (kg/mm^3)	Young's modulus (MPa)	Poisson's ratio	Yield stress (MPa)	tensile strength (MPa)
Ss316L	$7.8 \cdot 10^{-6}$	193000	0.27	207	606
CoCr L605	$9.7 \cdot 10^{-6}$	243000	0.3	476	1012
PtCr	$7.85 \cdot 10^{-6}$	203000	0.285	480	834

The behavior of the rubber balloon was modeled using a hyperelastic Mooney-Rivlin strain energy potential for polyurethane [46]. The values of the parameters in Mooney-Rivlin equation used in this investigation are listed in Table 3 [47].

The three-layered artery and plaque were modeled using the Ogden hyperelastic constitutive equation [18, 32]. The values of the parameters in Ogden equation used to model the behaviors of the three arterial layers and plaque are given in Table 4 [35].

2.3. Loading and boundary conditions

The FE simulations of stent deployment were performed using the ABAQUS CAE (Dassault Systèmes) FE software package. The type of loading was quasi-static and the problem was solved using implicit dynamics at three steps, i.e., (i) applying a blood pressure to the artery, (ii) loading by balloon inflation, and (iii) unloading by balloon deflation. At the first step, a constant internal pressure of 13.3 KPa (equal to 100 mm Hg [31]) was applied to the artery and plaque. The second step involved applying a pressure to inflate the balloon, expand the stent and immobilize it in the stenotic area. At this step, the balloon internal pressure increases from zero to 1.7 MPa in 0.1 sec, as illustrated in Fig. 4. At the third step, the balloon internal pressure was reduced to zero in 0.1 second, as the balloon deflated, while allowing the stent to recoil. Fig. 5 shows a diagram of the applied balloon pressure over time. The maximum pressure of 1.7 MPa was considered the nominal expansion pressure.

In the present FE simulations, the geometrical symmetry of the objects was utilized to reduce the computation time [38]. Instead of modeling the entire stent, balloon, artery section, and plaque, one-half were modeled. Appropriate boundary constraints were applied to the points on the symmetry surfaces by fixing the nodes there in the normal direction to the surface. In addition, the two ends of the balloon were fixed (fully constrained) with no rigid body motion. The nodes located at both ends of the artery and the plaque were allowed

Table 3- Mooney-Rivlin model coefficients for polyurethane balloon [47]

Material	ρ (kg/mm3)	C_{10} (MPa)	C_{01} (MPa)	D_1
Polyurethane	1.07×10^{-6}	1.03176	3 69266	0

Table 4- Coefficients of the Ogden hyperelastic model used to represent the material behaviors of the three arterial layers and hypocellular plaque [35]

Material	ρ (kg/mm3)	μ_1 (MPa)	μ_2 (MPa)	μ_3 (MPa)	α_1	α_2	α_3	D_1
Intima	1.07×10^{-6}	−7.04	4.23	2.85	24.48	25.00	23.54	8.95×10^{-7}
Media	1.07×10^{-6}	−1.23	0.88	0.45	16.59	16.65	16.5	5.31×10^{-6}
Adventitia	1.07×10^{-6}	−1.28	0.85	0.44	24.63	25.00	23.74	4.67×10^{-6}
hypocellular Plaque	1.45×10^{-6}	0.093	–	–	8.17	–	–	4.30×10^{-7}

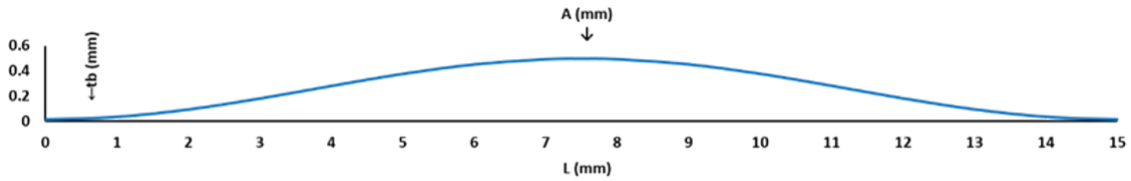

(a)

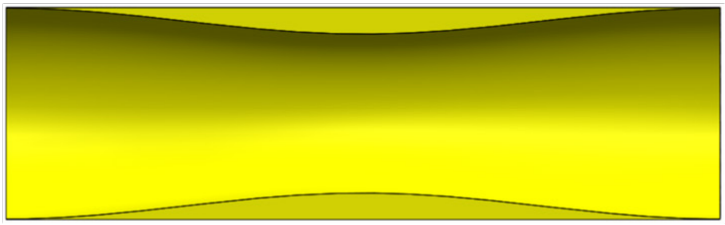

(b)

Fig. 4- Geometric specifications of the plaque: (a) drawing of the Hicks-Henne bump curve when A=0.5, xp=0.5, t=2, tb=0.01 and L=15 and (b) cross-sectional view of the plaque created based on the Hicks-Henne bump function.

to move, but only in the radial direction. The fixed constraint was applied between the plaque and artery and between the three layers of the artery. The interactions between the stent, the artery and the balloon were modeled as surface-to-surface hard contact with penalty friction. A friction coefficient of 0.25 was assumed [26].

2.4. Meshing

All the models were meshed using Abacus CAE. The stent was meshed using hexahedral elements with reduced integration and hourglass control (type C3D8R). Corresponding to the different stent designs, the total number of meshes were 97,676, 100,056, 155,725, 99,220 and 68,373 for

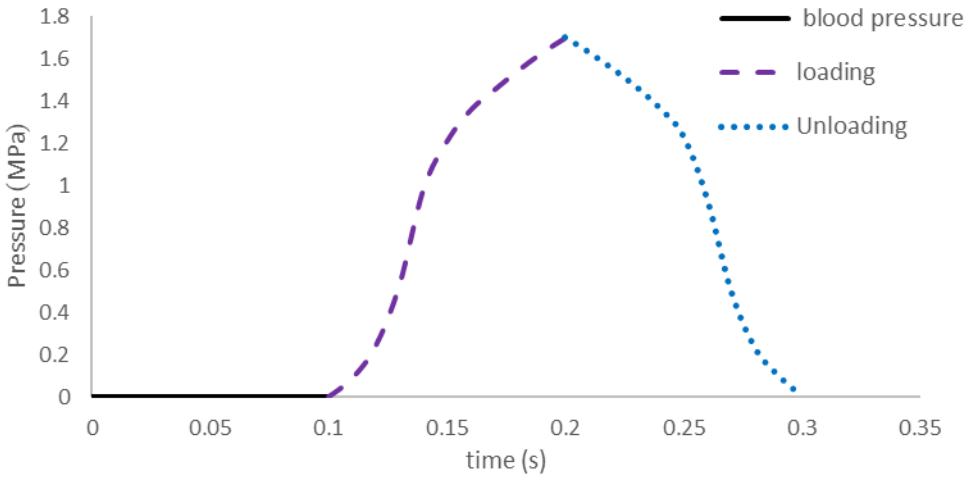

Fig. 5- Diagram of the balloon internal pressure over time.

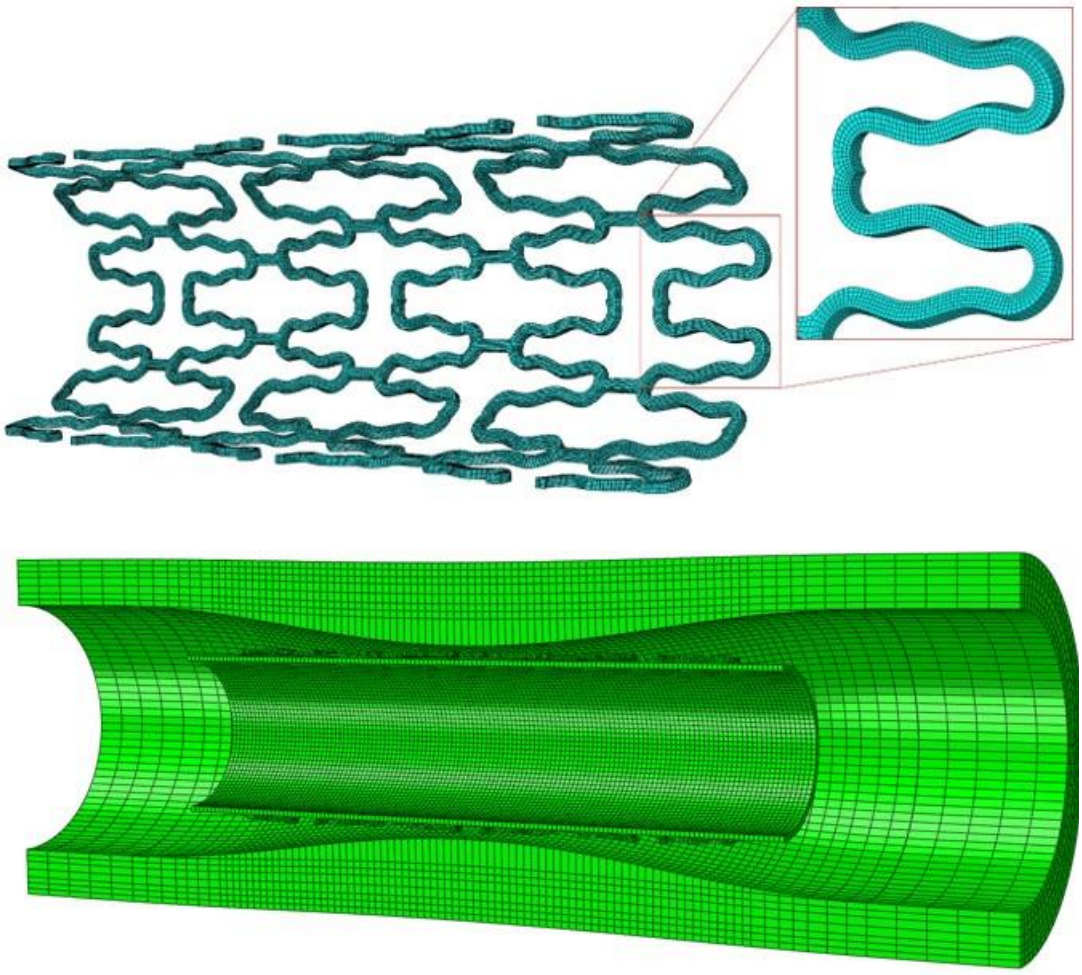

Fig. 6- Finite element meshes for the newly designed stent, artery, plaque and balloon.

the Palmaz-Schatz, NIR, BioMatrix, stent A and stent B, respectively. The balloon, artery and plaque were meshed using hexahedral elements with reduced integration and hourglass control. As these materials were assumed to be incompressible, a hybrid formula was used (type C3D8RH). The number of elements for the balloon, artery and plaque were 6,517, 31,234 and 4,002, respectively. As it can be seen in Fig. 6, denser meshes were created at the middle of the models where the stent, artery and plaque were in contact. With increasing distance from the middle to the side ends of the artery, the mesh density decreased. Sensitivity analysis was conducted by changing the number of elements in each model over a relatively large range. The optimum number of elements was chosen as the smallest number of elements, above which the variation in the maximum von Misses stress became negligible (less than 2%). In each run of simulation, the number of elements in one model was changed for one of the sub-models, i.e., the stent, artery or plaque, while it was kept unchanged for the rest of the sub-models. As a result, the convergence of results was confirmed for the new meshes.

2.5. Post-processing of results

The type of loading in this simulation was quasi-static. To confirm the validity of quasi-static, the internal energy and kinetic energy must be monitored, and the kinetic energy for the whole system must always be less than 5% of the internal energy. Fig. 7 shows a diagram of internal and kinetic energy over time during the simulation process. The proposal made by the developers of Abacus [50] guarantees a quasi-static process, and Gastaldi et al. [51] confirmed this quasi-static analysis validation.

The study of the artery von Mises stress is also important because research has shown that it is directly related to restenosis [52]. In fact, the more stress the stent exerts on the artery during deployment, the greater the risk of damage to the artery and consequent restenosis [52]. Restenosis after stenting means narrowing the artery again at the same site where the stent was previously implanted. This phenomenon, which is one of the main problems facing cardiovascular surgeons, is generally caused by injuries caused by stenting on artery during stenting [33, 45].

Three points of the stent (one point in the middle and two points at the end) were considered to calculate the expansion, recoil and dogboning. Expansion indicates an increase in the diameter of the stent compared to the initial diameter of the stent during balloon inflation, and the lower the amount of expansion at lower balloon pressure, the lower the risk of artery damage and restenosis. The maximum expansion is calculated based on the following equation [53]:

$$stent\ expansion\ = (\frac{R_{distal} - R_0}{R_0}) * 100$$

Where and R_0 are the distal radius of the stent at the end of loading or unloading step and the

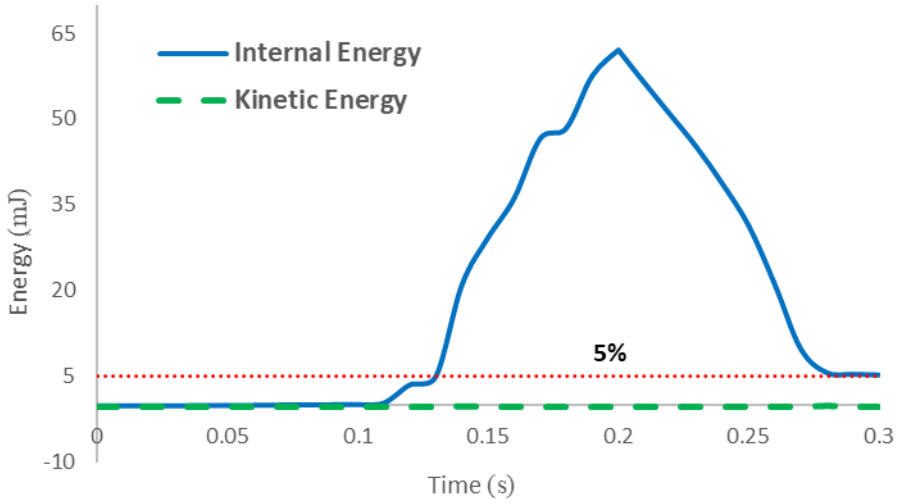

Fig. 7-Diagram of internal and kinetic energy over time during the simulation process.

initial radius of the stent before inflation of balloon, respectively. The recoil effect means a reduction in the diameter of the stent after the balloon exits, which occurs due to the resistance of the arterial wall. The lower the recoil, the higher the radial strength and the better the stent design. The recoil effect is calculated based on the following equation [53]:

$$Central\ radial\ recoil = \left(\frac{R_{central}^{loading} - R_{central}^{unloading}}{R_{central}^{loading}}\right) * 100$$

Where is the central radius of the stent at the end of the loading step and is the central radius of the stent at the end of the unloading step. The dogboning effect is the unequal expansion of the middle part of the stent relative to the free end, which occurs due to the presence of plaque in the middle of the stent and the free end of the two ends of the stent. In fact, the two free ends have a larger diameter than the middle part. This phenomenon can cause a lot of stress in the arterial walls. In fact, dogboning is one of the factors that increase the stress on the artery and leads to tissue damage and restenosis [52]. The dogboning effect is calculated based on the following equation [53]:

$$Dogboning\ = \left(\frac{R_{distal} - R_{central}}{R_{distal}}\right) * 100$$

3. Results and discussion

3.1. Stents design

In order to compare the design of the new hybrid stent (stent $A_{SS\ 316L}$) with the mentioned commercial stents, all the stents were simulated with stainless steel 316L material to examine only the design effect. The FEM simulations revealed the distributions of stresses in the stents after loading to a maximum pressure of 1.7 MPa and unloading, as shown in Fig. 8 and Fig. 9, respectively. The longitudinal and radial symmetries in stress distribution suggested proper modelling of the problem and application of the boundary conditions. It can be seen that the highest stress occurred at the corners or at the U-bends and W-bends of the struts, which is in line with observation of Gu et al. [52] and Schiavone et al. [37]. The expansion of the stent occurred by stretching the struts. In addition to a higher level of deformation, the areas at the corners or bends were subjected to high stresses. However, as can be seen in Fig. 8, in none of the stents, the maximum stress exceeded the ultimate tensile strength (UTS) of SS 316L (606 MPa). It was also observed that the new hybrid stent did not fail under these quasi-static loading conditions.

The distribution of stresses in the artery-plaque system at the end of the unloading step is shown in Fig. 10. The highest stress was also applied to the intima layer, i.e., the inner layer of the artery. In the study conducted by Schiavone et al. [37], such a stress distribution was attributed to the higher strength of the intima layer surrounded by the other layers. A pattern of longitudinal and radial symmetries in stress distribution in the artery, similar to that observed in the stent, was observed, indicating trustable predictions of the FE simulations. The maximum stresses on the artery-plaque system at the end of the unloading step for the Palmaz-Schatz, NIR, BioMatrix and the stent $A_{SS\ 316L}$ were 0.165, 0.185, 0.27 and 0.213 MPa, respectively. At this step, the open-cell stent (BioMatrix) exerted higher stresses on the artery than the closed-cell stents and hybrid stent $A_{SS\ 316L}$. Also, the stresses applied to the artery-plaque system by the stents at the end of the unloading step in this study are less than the ultimate tensile stresses for the artery (0.394 + 0.223 MPa according to the studies of Holzapfel et al. [54]), which can reduce the risk of artery damage and restenosis. This is also true for hybrid stent $A_{SS\ 316L}$.

The maximum expansions were respectively 76.27, 76.70, 81.1 and 80.89 % for the Palmaz-Schatz, NIR, BioMatrix and stent $A_{SS\ 316L}$, under a balloon pressure of 1.7 MPa. Corresponding to these values, the maximum diameter of the BioMatrix stent at the end of the loading step was 5.43 mm and those of the stent $A_{SS\ 316L}$, NIR and Palmaz-Schatz were to 5.42, 5.30 and 5.28 mm, respectively. Clearly, the open-cell stent had a larger maximum expansion than the closed-cell and hybrid stents. This indicates the important role of open-cells in determining the extent of stent expansion. Under a given balloon pressure, a lower maximum expansion of a closed-cell stent means a higher radial stiffness, which is an important parameter for the stent to stay in place after the balloon is deflated. On the other hand, a lower pressure would be required to expand an open-cell stent to achieve a desired diameter. The studies carried out by Schiavone et al. [37] also showed that open-cell stents expanded more easily than the closed-cell counterparts. According to the obtained results, hybrid stent $A_{SS\ 316L}$ has a maximum expansion very close to open-cell stent, which has the largest maximum expansion. Fig. 11

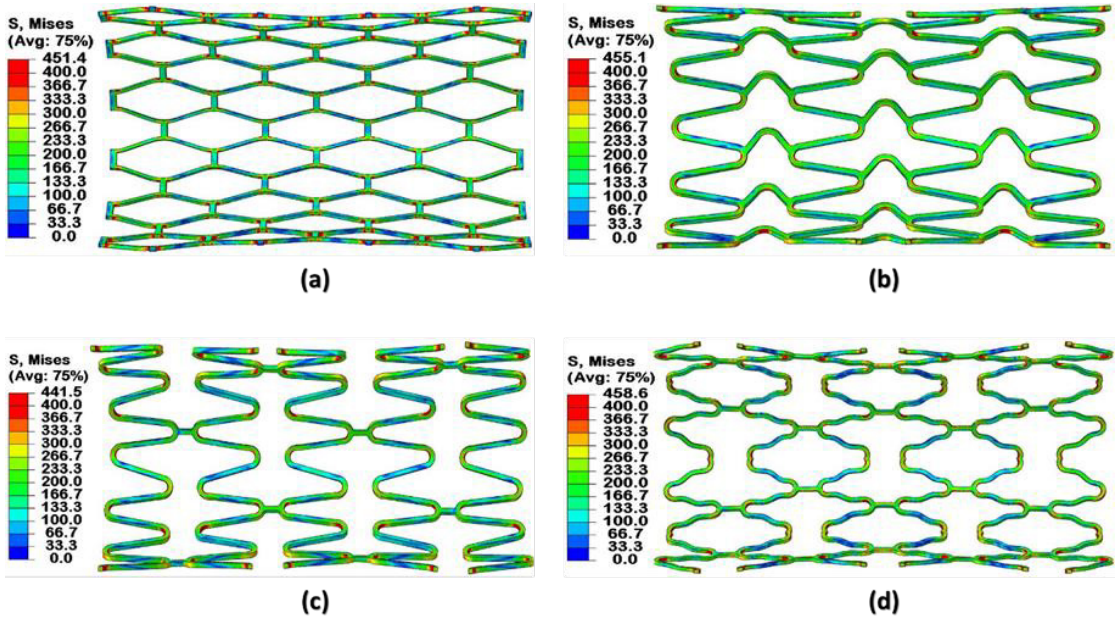

Fig. 8- The von Mises stress distribution for (a) Palmaz-Schatz, (b) NIR, (c) BioMatrix and (d) stent A SS 316L stents at the end of the loading step.

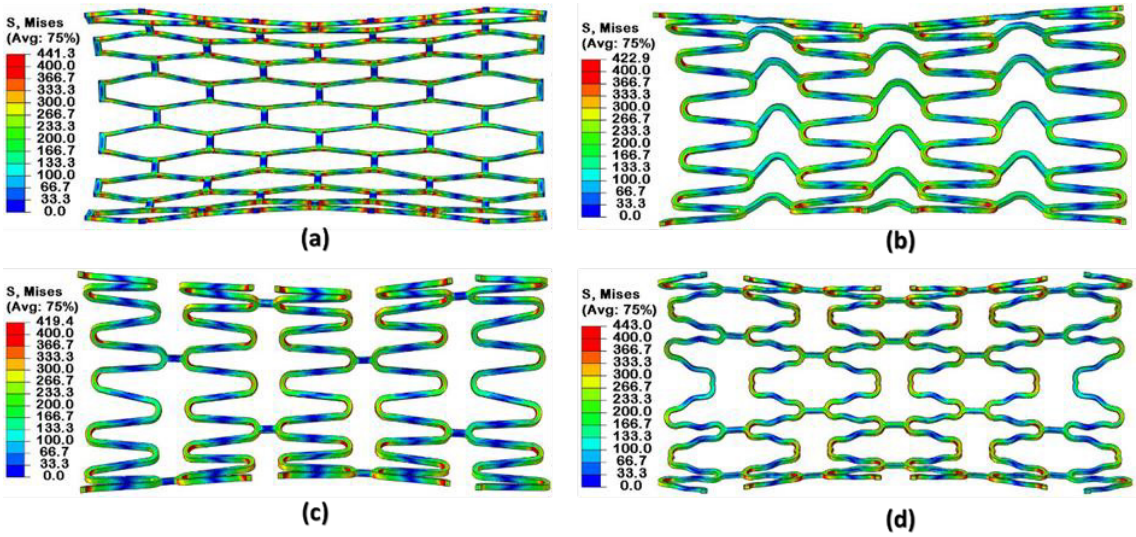

Fig. 9- The von Mises stress distribution for (a) Palmaz-Schatz, (b) NIR, (c) BioMatrix and (d) stent A SS 316L stents at the end of the unloading step.

shows simulation of the required pressure for stent expansion throughout a full cycle of loading and then unloading. It can be seen that the required pressure increases from zero to a maximum (1.7 MPa for all the stents) during the loading step of the cycle when the maximum stent diameter was achieved. During unloading when the balloon pressure was released, the diameter of the stent decreased under the action of the back pressure of the artery wall. This process is called stent recoil.

The values of recoil of the Palmaz-Schutz, NIR, BioMatrix and stent $A_{SS\ 316L}$ were 22.23, 21.50, 20.57 and 21.36 %, respectively. Clearly, the open-cell stent exhibited less recoil than the closed-cell and hybrid stents, as found by Migliawaka et al. [20] and Park et al. [28]. Although the values of recoil of stents is close to each other, hybrid stent $A_{Ss\ 316L}$ did not show very good results compared to closed-cell stents.

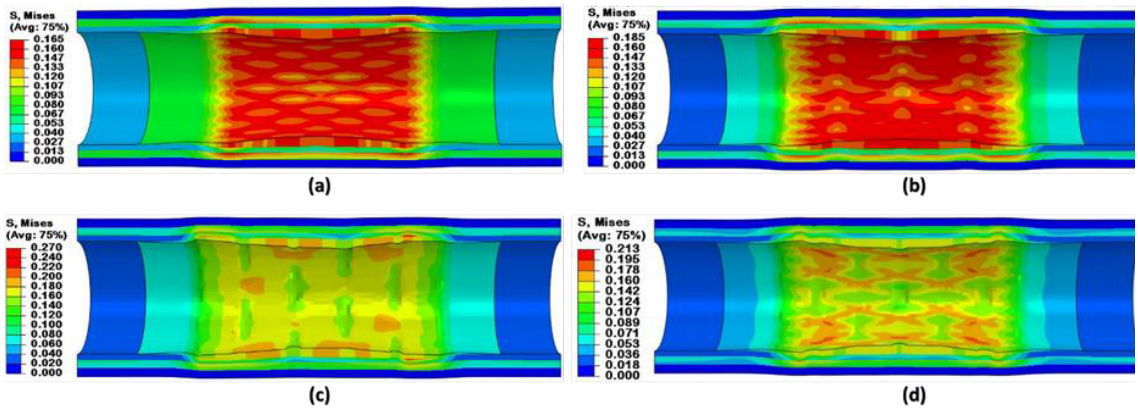

Fig. 10- The von Mises stress distribution in the artery-plaque system distribution for (a) Palmaz-Schatz, (b) NIR, (c) BioMatrix and (d) stent A SS 316L stents at the end of the unloading step.

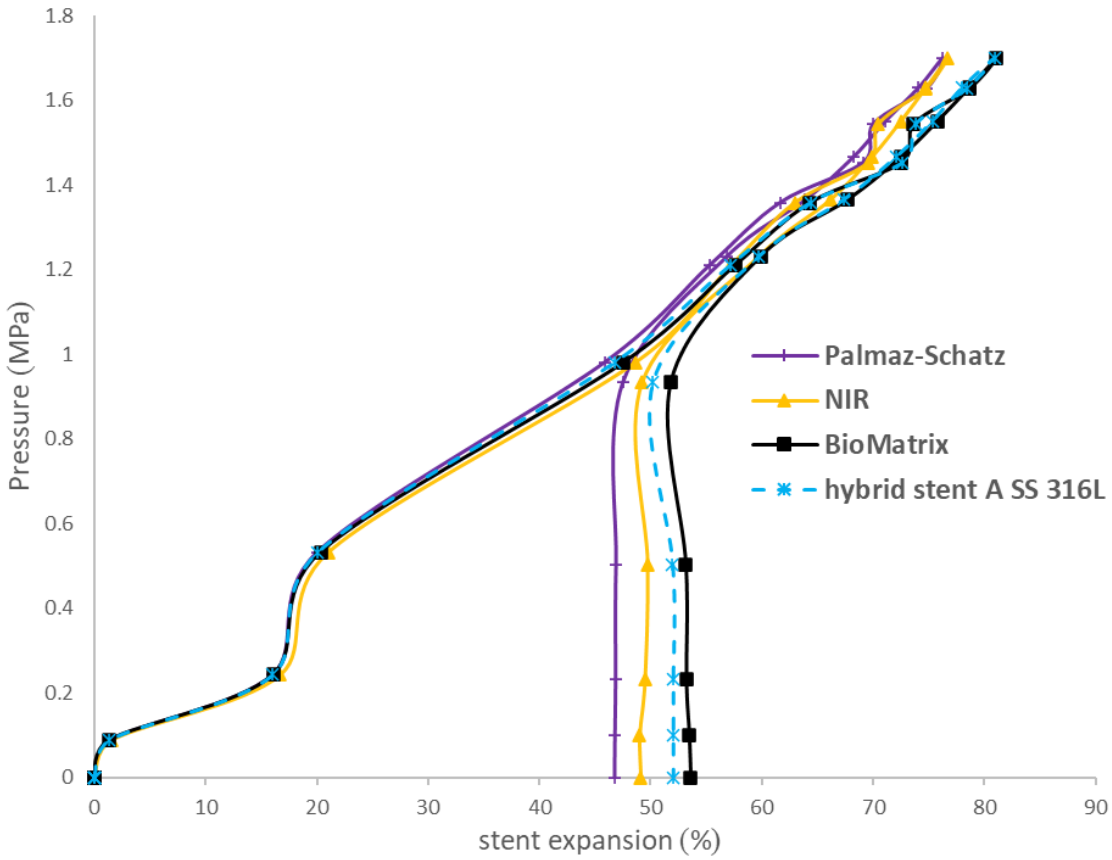

Fig. 11- Simulation of required pressure for stent expansion in a full loading-unloading cycle for Palmaz-Schatz, NIR, BioMatrix and stent A Ss 316L.

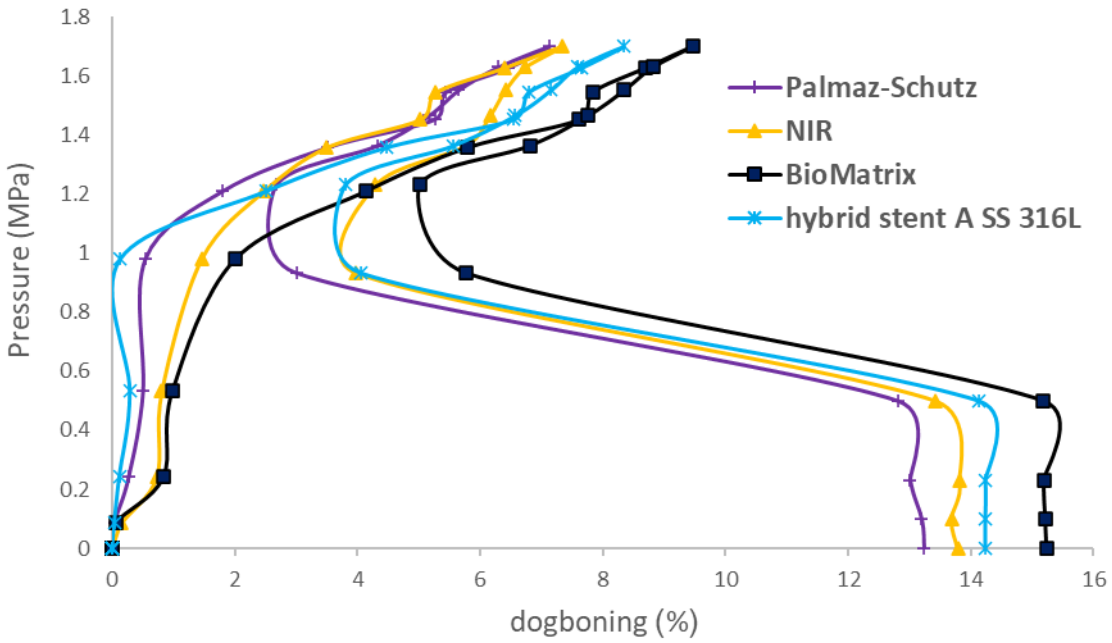

Fig. 12- Diagram showing the variation of dogboning with balloon pressure for Palmaz-Schatz, NIR, BioMatrix and hybrid stent A Ss 316L.

The dogboning values calculated for the Palmaz-Schatz, NIR, BioMatrix and stent A $_{SS\ 316L}$ at the end of the loading step were 7.13, 7.34, 9.46 and 8.34 % while those at the end of the unloading step were 13.23, 13.79, 15.24 and 14.23 %, respectively. These values indicated that the open-cell stent had a stronger dogboning effect in comparison with the closed-cell and hybrid stent A $_{SS\ 316L}$, as found by Schiavone et al [36]. The results show that hybrid stent A $_{SS\ 316L}$ has dogboning values between closed-cell and open-cell stents. Fig. 12 shows a diagram correlating the dogboning percentage with applied balloon pressure throughout one full cycle of loading and unloading. The dogbonning was zero before the start of loading. With increasing balloon pressure during loading toward the maximum pressure of 1.7 MPa, the percentage of dogbonning kept rising. The dogboning started to reduce at the onset of unloading. However, the most significant dogboning occurred at the end of the unloading step, due to the eliminated balloon pressure (i.e. balloon deflating) and the pressures acted by the artery wall and plaque. By comparing Fig. 8 and Fig. 9, showing the stress distributions of the stent at the end of the loading and unloading steps, respectively, one could clearly see that the effect of the dogboning increased at the end of the unloading step.

3.2. Effects of material type

The FEM simulations revealed the distributions of stresses in the stent A $_{SS\ 316L}$, stent A $_{CoCr\ L605}$ and stent A $_{PtCr}$ after loading to a maximum pressure of 1.7 MPa and after unloading to investigate the material change from SS 316L to CoCr L605 and PtCr, as shown in Fig. 13 and Fig. 14, respectively. The stress distribution for stent A $_{SS\ 316L}$, stent A $_{CoCr\ L605}$ and stent A $_{PtCr}$, is the same at the end of the loading step, the highest maximum stress is related to stent A $_{CoCr\ L605}$ (716.3 MPa) and the lowest maximum stress is related stent A $_{SS\ 316L}$ (458.6 MPa) while the maximum stress in stent A $_{PtCr}$ is 668.6 MPa (see Fig. 13). It can be seen the maximum stress in any of the stents was not higher than the UTS of SS 316L (606 MPa), CoCr (1012 MPa) and PtCr (834 MPa), which indicates that the risk of failure is low in all stents. This shows that all three materials selected for new design stent A can be suitable. The stress distribution for stent A $_{SS\ 316L}$, stent A $_{CoCr\ L605}$ and stent A $_{PtCr}$, is the same at the end of the unloading step, with the highest stress related to stent A $_{CoCr\ L605}$ (722.2 MPa) and the lowest stress related to stent A $_{Ss\ 316L}$ (443 MPa) while the stress in stent A $_{PtCr}$ is 668.6 MPa (see Fig. 14). The order of maximum stresses and stresses at the end of the loading step has also been confirmed based on the study of Conway et al. [17].

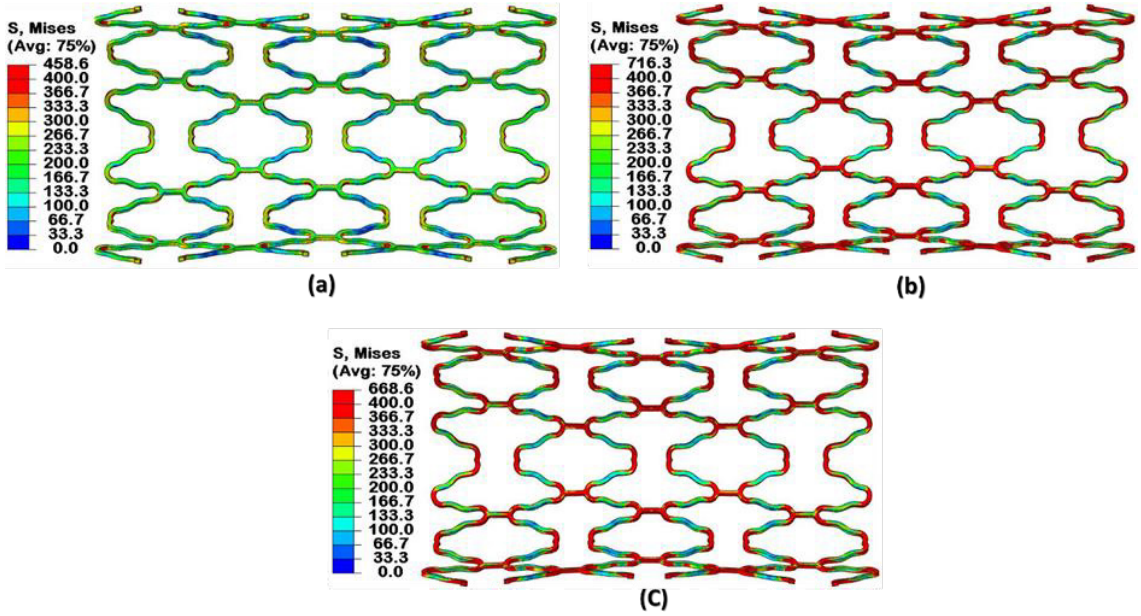

Fig. 13- The von Mises stress distribution for (a) stent A SS 316L, (b) stent A CoCr L605 and (c) stent A PtCr at the end of the loading step.

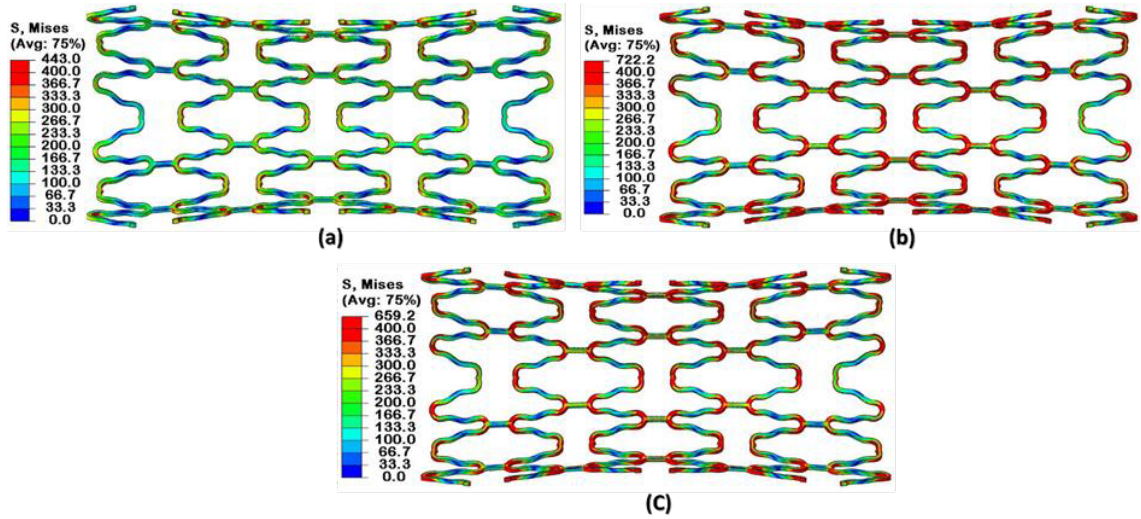

Fig. 14- The von Mises stress distribution for (a) stent A SS 316L, (b) stent A CoCr L605 and (c) stent A PtCr at the end of the unloading step.

The stress distribution in the artery-plaque system stent $A_{SS\ 316L}$, stent $A_{CoCr\ L605}$ and stent A_{PtCr} at the end of the unloading step (see Fig. 15) is the same and shows that most of the stress enters the intima layer. The stress of the artery-plaque system at the end of the unloading step for stent $A_{SS\ 316L}$, stent $A_{CoCr\ L605}$ and stent A_{PtCr} are 0.213, 0.422 and 0.380 MPa respectively this indicates that the SS 316L stent causes less restenosis than the other two stents. The highest artery-plaque system stress occurred in stent $A_{CoCr\ L605}$ and the lowest stress occurred in the SS 316L stent, which was confirmed in a similar study by Conway et al. [17] and Schiavone et al. [37].

Fig. 16 shows a diagram of stent expansion changes at different pressures during the loading and unloading step, with a pressure of 1.7 showing the maximum stent expansion. Investigation of the material effect on the maximum expansion of the new stents, which occurs at a pressure of 1.7 MPa,

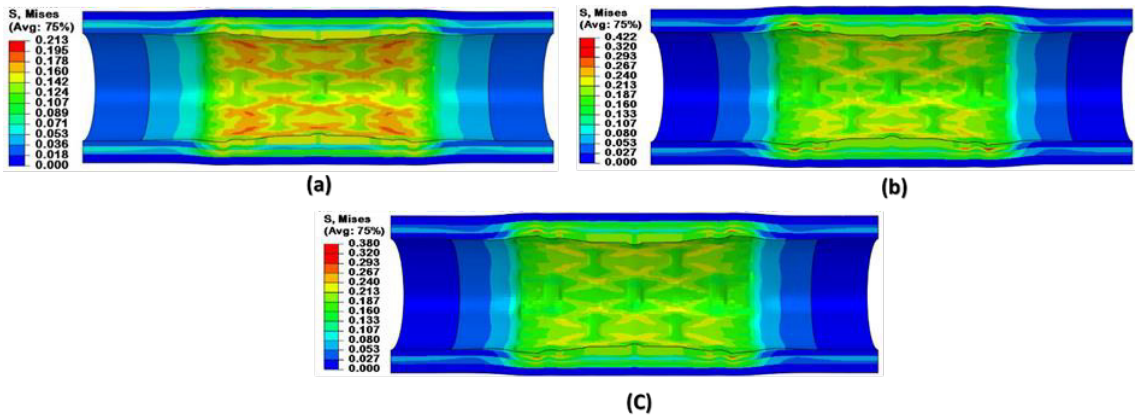

Fig. 15- The von Mises stress distribution for artery-plaque system at the end of the unloading step (a) stent A SS 316L, (b) stent A CoCr L605 and (c) stent A PtCr.

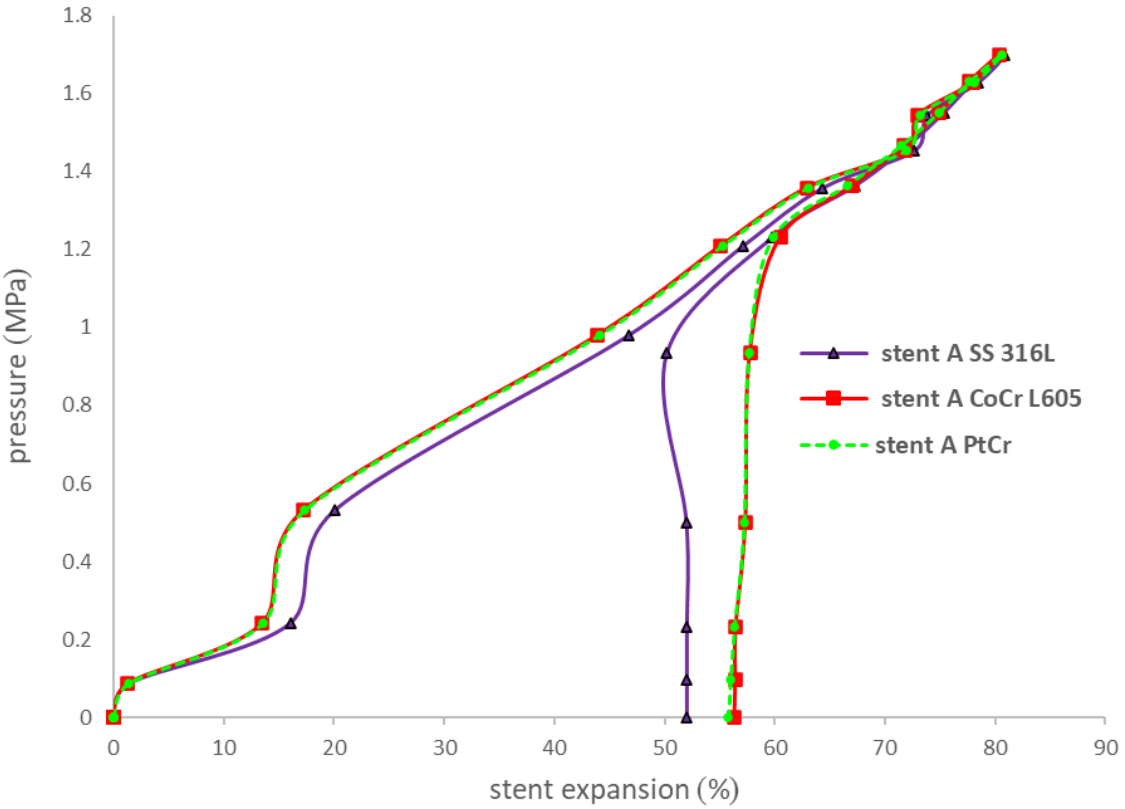

Fig. 16- Stent expansion changes at different of pressures for stent A SS 316L, stent A CoCr L605 and stent A PtCr.

showed that stent $A_{SS\ 316L}$ have a higher maximum expansion (80.89 %) compared to stent $A_{CoCr\ L605}$ (80.44%) and stent A_{PtCr} (80.57%). However, the difference in the maximum amount of expansion between the three stents was very small. In the unloading step, due to the reduction of the balloon pressure and the pressure of the arterial wall, the amount of stents expansion decreases, which indicates the recoil of the stent. At the end of the unloading step, it is observed that the expansion in the stent $A_{SS\ 316L}$ (52%) is less than that in stent $A_{CoCr\ L605}$ (56.4%) and stent A_{PtCr} (55.8%). This is due to the difference in recoil stents, which will be discussed in the next section.

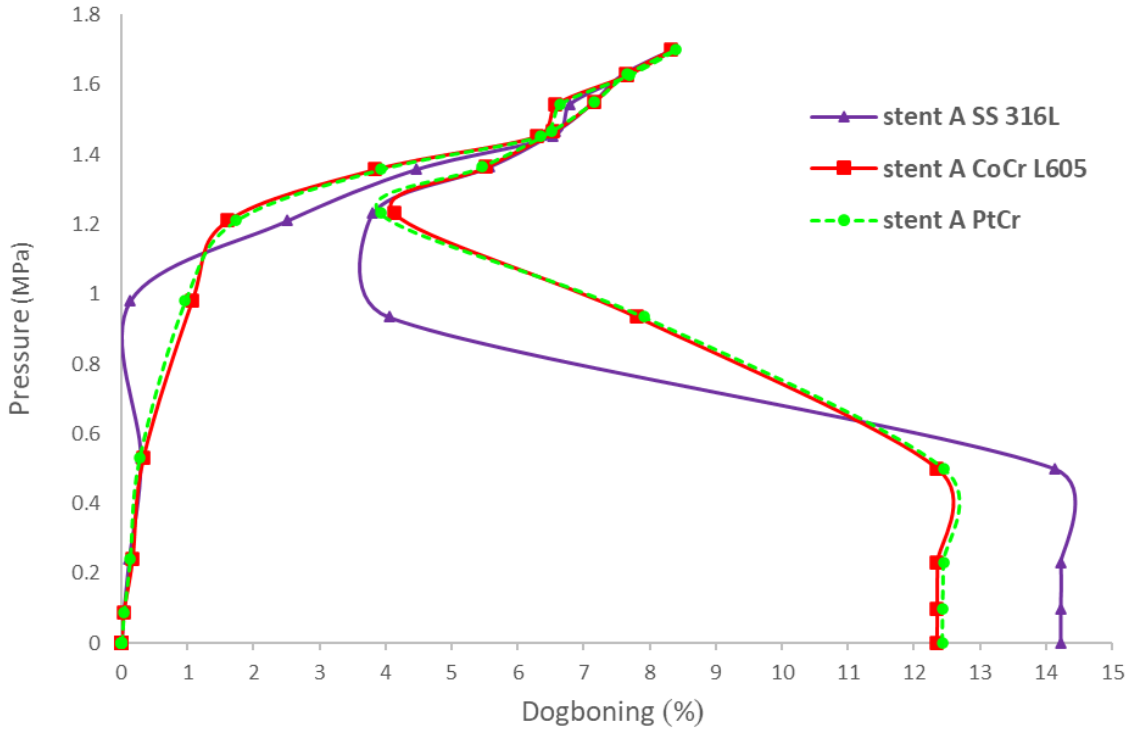

Fig. 17- Diagram of dogboning change in terms of pressure for stent A SS 316L, stent A CoCr L605 and stent A PtCr.

The material effect on the recoil of the new stents showed that the stent A $_{SS\ 316L}$ has a higher recoil (21.36%) compared to the stent A $_{CoCr\ L605}$ (17.13%) and the stent A $_{PtCr}$ (17.53%). In fact, the results show that the radial strength of the stent A $_{SS\ 316L}$ is lower than the other two stents. Schiavone et al. [37] also found that materials with lower yield stress had higher recoil. The greater recoil on the SS 316L stent compared to the CoCr L605 and PtCr stents resulted in a larger expansion and final diameter of the SS 316L stent compared to the other two stents. By comparing Fig. 14 with Fig. 13, can be seen the recoil of the stents, due to this effect, the diameter of the stent has decreased after deflation of the balloon at the end of the unloading step.

Examination of material effect on the dogboning affect are shown in the diagram in Fig. 17. In this figure, changes in the dogboning effect are shown based on the changes in pressure on the balloon. Fig. 17 shows that stent A $_{SS\ 316L}$, stent A $_{CoCr\ L605}$ and stent A $_{PtCr}$ at the maximum balloon pressure of the 1.7 MPa (end of the loading step) have an approximately equal dogboning effect of 8.34, 8.33 and 8.38, respectively. However, in the continuation and reaching the end of the unloading step, the amount of dogboning increases for all three stents, which is due to the increase in the pressure of the arterial wall and plaque after balloon deflation. The amount of dogboning for the stent A $_{SS\ 316L}$, stent A $_{CoCr\ L605}$ and stent A $_{PtCr}$ at the end of the unloading step is 14.23, 12.34 and 12.43, respectively. By comparing Fig. 13 and Fig. 14, showing the stress distributions of the stent at the end of the loading and unloading steps, respectively, one could clearly see that the effect of the dogboning increased at the end of the unloading step which causes the diameter in the center of the stent to decrease compared to the two ends of the stent. In fact, stent A $_{SS\ 316L}$ has the greatest dogboning effect. Studies by Schiavone et al. [37] showed that SS 316L stents had a greater dogboning effect than CoCr L605 stents.

3.3. Investigation of reduction Thickness of Struts

By comparing a new stent B (stent with less thickness at the struts) with new stent A in two materials CoCr L605 and PtCr, it was found that the distribution of Von Mises stress and maximum stress did not change much with decreasing the thickness of the struts (Fig. 18). However, in the study of stress in the artery-plaque system (Fig. 19), stress in stent B $_{CoCr\ L605}$ (0.422 MPa) and stent B $_{PtCr}$ (0.380 MPa) is reduced compared to stent A $_{CoCr\ L605}$

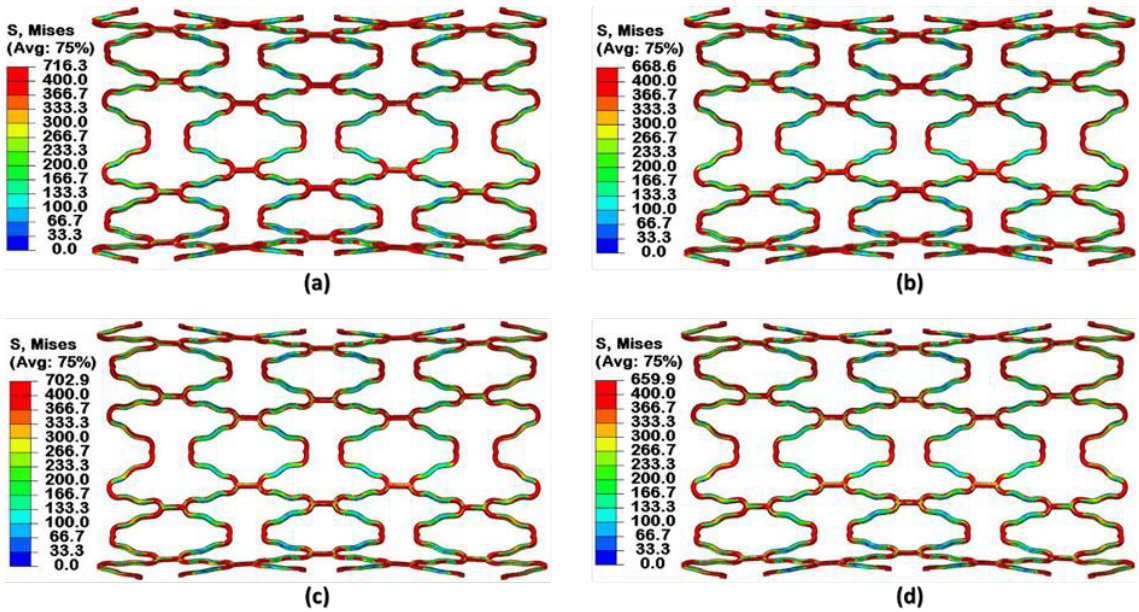

Fig. 18- The von Mises stress distribution for (a) stent A CoCr L605, (b) stent A PtCr, (c) stent B CoCr L605 and (d) stent B PtCr at the end of the loading step.

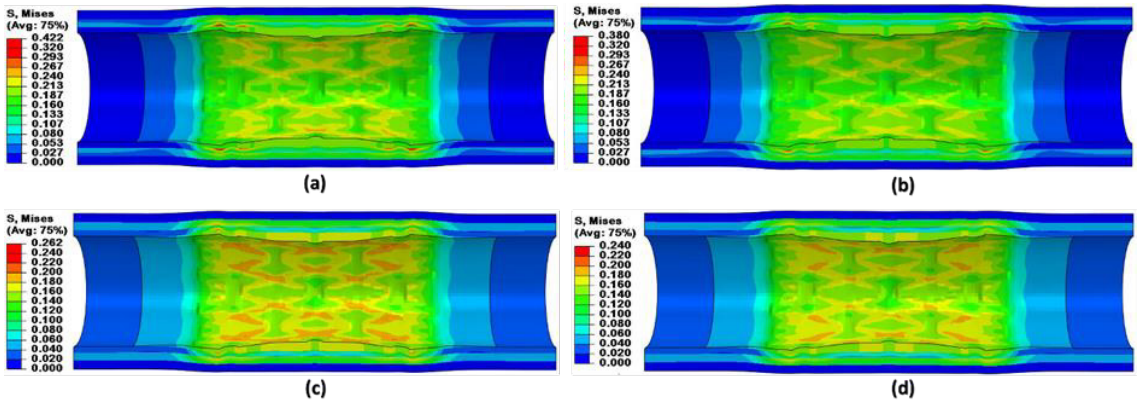

Fig. 19- The von Mises stress distribution for artery-plaque system at the end of the unloading step for (a) stent A CoCr L605, (b) stent A PtCr, (c) stent B CoCr L605 and (d) stent B PtCr.

(0.262 MPa) and stent A $_{PtCr}$ (0.240 MPa). Studies by Zahedmanesh et al. [35] and Gijsen et al. [55] also showed that reducing the thickness of the Haas stent base reduces the stress on the artery.

Investigation of the Thickness effect on the maximum expansion of the new stents, showed that stent B $_{CoCr\ L605}$ (81.95%) and stent B $_{PtCr}$ (82.11%) have a higher maximum expansion compared to stent A $_{CoCr\ L605}$ (80.44%) and stent A $_{PtCr}$ (80.57%). Fig. 20 shows a diagram of stent expansion changes at different pressures during the loading and unloading step. It can be seen that at the end of the unloading step, the expansion in stent B $_{CoCr\ L605}$ (56.01%) and stent B $_{PtCr}$ (54.28%) decreases compared to stent A $_{CoCr\ L605}$ (56.4%) and stent A $_{PtCr}$ (55.8%), which may be due to an increase in recoil due to a decrease in thickness of struts. Examination of recoil shows that in stent B $_{CoCr\ L605}$ (19.54%) and stent B $_{PtCr}$ (19.94%) compared to stent A $_{CoCr\ L605}$ (17.13%) and stent A $_{PtCr}$ (17.53%), the amount of recoil increases with decreasing thickness of struts. It can be seen that the thickness

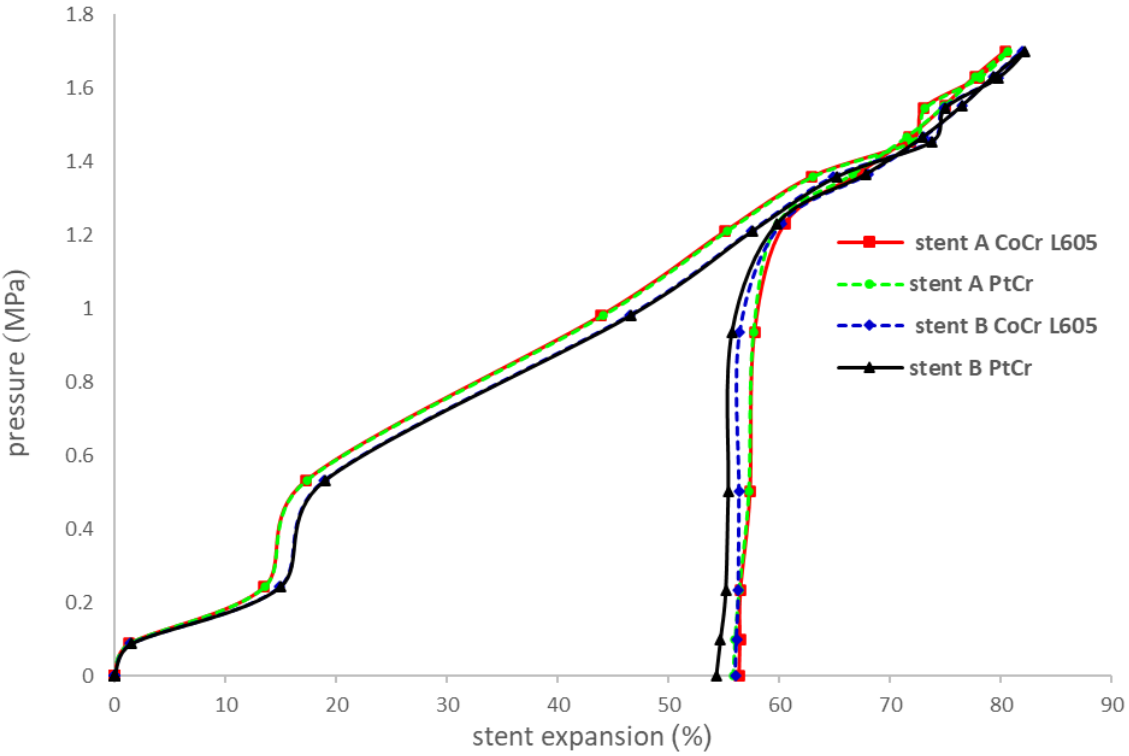

Fig. 20- Stent expansion diagram in terms of pressure for stent A CoCr L605, stent A PtCr, stent B CoCr L605 and stent B PtCr.

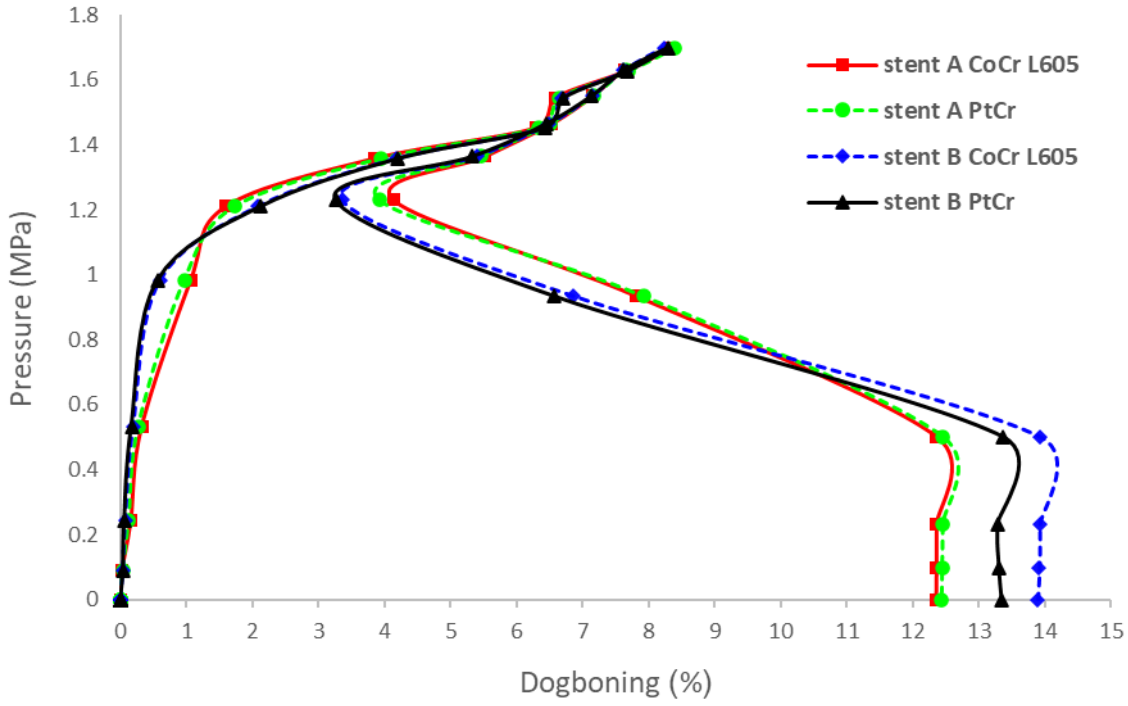

Fig. 21- Diagram of dogboning change in terms of pressure (During the loading and unloading steps) for stent A CoCr L605, stent A PtCr, stent B CoCr L605 and stent B PtCr.

of struts has a significant effect on the recoil.

Investigation of the effect of Thickness on the dogboning effect are shown in Fig. 21, which shows the changes in the dogboning effect based on the changes in pressure on the balloon. Fig. 21 shows that stent $B_{CoCr\ L605}$, stent B_{PtCr}, stent $A_{CoCr\ L605}$ and stent A_{PtCr} at the end of the loading step (the maximum pressure of the 1.7 MPa balloon) have an approximately equal dogboning effects of 8.23, 8.29, 8.33 and 8.38%, respectively. At the end of the unloading step, the amount of dogboning increases for all stents. The amount of dogboning for stent $B_{CoCr\ L605}$, stent B_{PtCr}, stent $A_{CoCr\ L605}$ and stent A_{PtCr} at the end of the unloading step is 13.89, 13.34, 12.34 and 12.43%, respectively, which shows that reducing the thickness of the struts increases the dogboning in the stents.

4. Conclusions

Biomechanical behaviors of the open cell, closed cell and new hybrid stents as well as the effect of changing the material (stainless steel 316L to CoCr alloy and PtCr alloy) and reduction in thickness of struts on biomechanical behaviors of new hybrid stents are investigated by constructing a balloon-stent-artery model, including three artery layers and a plaque, and performing FE simulations. Blood pressure of 100 mm Hg was also applied to the artery–plaque system. According to this investigation the following conclusions are made:

- The new hybrid stent design performed at least as well as the commercial open-cell and closed-cell stents in terms of biomechanical parameters like maximum expansion, recoil, and dogboning.
- Changing the stent material from stainless steel to cobalt-chromium or platinum-chromium alloys improved the biomechanical behavior, increasing expansion, reducing recoil, and decreasing dogboning. However, it also led to an increase in maximum stress on the artery-plaque system.
- Reducing the stent strut thickness from 0.1 mm to 0.08 mm decreased the maximum stress on the artery-plaque system, but undesirably increased dogboning and recoil.
- The comprehensive finite element modeling approach provided valuable insights into the detailed biomechanical responses, but experimental validation and long-term clinical data would be needed to fully confirm the findings.

References

1. S. Motamed, S. N. Hosseini Karimi, M. Hooshyar, R. Mehdinavaz Aghdam, Advances in nanocarriers as drug delivery systems in Atherosclerosis therapy, Journal of ultrafine grained and nanostructured materials, Volume 54, 2021, 198-210.
2. M. Shabani, G. Faraji, Processing and Characterization of Natural Hydroxyapatite Powder from Bovine Bone, Journal of ultrafine grained and nanostructured materials, Volume 53, 2020, 204-209.
3. H. Mirzadeh, Superplasticity of fine-grained austenitic stainless steels: A review, Journal of ultrafine grained and nanostructured materials, Volume 56, 2023, 27-41.
4. N. Mollaei, S. M. Fatemi, M. Abootalebi, H. Razavi, Zinc based bioalloys processed by severe plastic deformation – A review, Journal of ultrafine grained and nanostructured materials, Volume 53, 2020, 39-47.
5. R. Sarvari, M. Nouri, L. Roshangar, M. S. Gholami Farashah, A. Sadrhaghighi, S. Agbolaghi, P. Keyhanvar, Conductive Bio-Copolymers based on Pectin-Polycaprolactone/Polyaniline and Tissue Engineering Application Thereof, Journal of ultrafine grained and nanostructured materials, Volume 54, 2021, 64-72.
6. G. A. Roth et al., "Global, Regional, and National Burden of Cardiovascular Diseases for 10 Causes, 1990 to 2015.," J. Am. Coll. Cardiol., vol. 70, no. 1, pp. 1–25, Jul. 2017, doi: 10.1016/j.jacc.2017.04.052.
7. WHO, "About cardiovascular diseases. Geneva: World Health Organization," 2019. Available: https://www.who.int/cardiovascular_diseases/about_cvd/en/.
8. R. Chronic et al., Diet and health: implications for reducing chronic disease risk, vol. 27, no. 06. 1990.
9. G. N. Levine et al., "2011 ACCF/AHA/SCAI guideline for percutaneous coronary intervention," J. Am. Coll. Cardiol., vol. 58, no. 24, pp. e44–e122, 2011, doi: 10.1016/j.jacc.2011.08.007.
10. D. Stoeckel, C. Bonsignore, and S. Duda, "A survey of stent designs," Minim. Invasive Ther. Allied Technol., vol. 11, no. 4, pp. 137–147, Jan. 2002, doi: 10.1080/136457002760273340.
11. I. Aneta, "Numerical analysis of mechanical phenomena in coronary stent made of titanium alloy Ti-13Nb-13Zr," vol. 687, pp. 191–198, 2016, doi: 10.4028/www.scientific.net/KEM.687.191.
12. T. Wu and S. Mccarthy, "Coronary Arterial Drug-Eluting Stent : From Structure to Clinical," 1900.
13. S. K. Jaganathan, E. Supriyanto, S. Murugesan, A. Balaji, and M. K. Asokan, "Biomaterials in Cardiovascular Research: Applications and Clinical Implications," Biomed Res. Int., vol. 2014, p. 11, 2014, doi: 10.1155/2014/459465.
14. B. J. O'Brien, J. S. Stinson, S. R. Larsen, M. J. Eppihimer, and W. M. Carroll, "A platinum-chromium steel for cardiovascular stents," Biomaterials, vol. 31, no. 14, pp. 3755–3761, 2010, doi: 10.1016/j.biomaterials.2010.01.146.
15. Safavi MS, Khalil-Allafi J, Ahadzadeh I, Walsh FC, Visai L. Improved corrosion protection of a NiTi implant by an electrodeposited HAp-Nb2O5 composite layer. Surface and Coatings Technology. 2023 Oct 15;470:129822.
16. K. Maleckis, E. Anttila, P. Aylward, W. Poulson, A. Desyatova, J. MacTaggart, A. Kamenskiy, Nitinol Stents in the Femoropopliteal Artery: A Mechanical Perspective on Material, Design, and Performance, Annals of biomedical engineering, 2018, Volume 46, pages 684–704.
17. C. Conway, E. R. Edelman, G. S. Karanasiou, N. S. Tachos, and L. K. Michalis, "In silico assessment of the effects of material on stent deployment," pp. 462–467, 2017, doi: 10.1109/BIBE.2017.00084.
18. S. Georgia Karanasiou et al., "In Silico analysis of stent deployment- effect of stent design," Proc. Annu. Int. Conf. IEEE

Eng. Med. Biol. Soc. EMBS, vol. 2018-July, pp. 4567–4570, 2018, doi: 10.1109/EMBC.2018.8513205.
19. C. Dumoulin and B. Cochelin, "Mechanical behaviour modelling of balloon-expandable stents," J. Biomech., vol. 33, no. 11, pp. 1461–1470, Nov. 2000, doi: 10.1016/S0021-9290(00)00098-1.
20. F. Migliavacca, L. Petrini, M. Colombo, F. Auricchio, and R. Pietrabissa, "Mechanical behavior of coronary stents investigated through the finite element method," J. Biomech., vol. 35, no. 6, pp. 803–811, Jun. 2002, doi: 10.1016/S0021-9290(02)00033-7.
21. S. N. D. Chua, B. J. Mac Donald, and M. S. J. Hashmi, "Finite-element simulation of stent expansion," J. Mater. Process. Technol., vol. 120, no. 1–3, pp. 335–340, Jan. 2002, doi: 10.1016/S0924-0136(01)01127-X.
22. S. N. David Chua, B. J. Mac Donald, and M. S. J. Hashmi, "Finite element simulation of stent and balloon interaction," J. Mater. Process. Technol., vol. 143–144, pp. 591–597, Dec. 2003, doi: 10.1016/S0924-0136(03)00435-7.
23. S. N. D. Chua, B. J. MacDonald, and M. S. J. Hashmi, "Effects of varying slotted tube (stent) geometry on its expansion behaviour using finite element method," J. Mater. Process. Technol., vol. 155–156, no. 1–3, pp. 1764–1771, Nov. 2004, doi: 10.1016/j.jmatprotec.2004.04.395.
24. W. Q. Wang, D. K. Liang, D. Z. Yang, and M. Qi, "Analysis of the transient expansion behavior and design optimization of coronary stents by finite element method," J. Biomech., vol. 39, no. 1, pp. 21–32, 2006.
25. Z. Xia, F. Ju, and K. Sasaki, "A general finite element analysis method for balloon expandable stents based on repeated unit cell (RUC) model," Finite Elem. Anal. Des., vol. 43, no. 1, pp. 86–95, 2007, doi: 10.1016/j.finel.2007.01.001.
26. F. Ju, Z. Xia, and K. Sasaki, "On the finite element modelling of balloon-expandable stents," J. Mech. Behav. Biomed. Mater., vol. 1, no. 1, pp. 86–95, Jan. 2008, doi: 10.1016/j.jmbbm.2007.07.002.
27. D. Lim, S.-K. Cho, W.-P. Park, A. Kristensson, J.-Y. Ko, and S. T. S. Al-Hassani, "Suggestion of Potential Stent Design Parameters to Reduce Restenosis Risk driven by Foreshortening or Dogboning due to Non-uniform Balloon-Stent Expansion," Ann. Biomed. Eng., vol. 36, no. 7, pp. 1118–1129, Jul. 2008, doi: 10.1007/s10439-008-9504-1.
28. W. Park, S. Cho, J. Ko, A. Kristensson, H. Kim, and D. Lim, "Evaluation of Stent Performances using FEA considering a Realistic Balloon Expansion," Eng. Technol., vol. 2, no. 1, pp. 117–122, 2008.
29. A. Kumar and N. Bhatnagar, "Finite element simulation and testing of cobalt-chromium stent: a parametric study on radial strength , recoil , foreshortening , and dogboning," Comput. Methods Biomech. Biomed. Engin., vol. 0, no. 0, pp. 1–15, 2020, doi: 10.1080/10255842.2020.1822823.
30. W. Walke, Z. Paszenda, and J. Filipiak, "Experimental and numerical biomechanical analysis of vascular stent," J. Mater. Process. Technol., vol. 164–165, no. 1263–1268, pp. 1263–1268, May 2005, doi: 10.1016/j.jmatprotec.2005.02.204.
31. C. Lally, F. Dolan, and P. J. Prendergast, "Cardiovascular stent design and vessel stresses: a finite element analysis," J. Biomech., vol. 38, no. 8, pp. 1574–1581, Aug. 2005, doi: 10.1016/j.jbiomech.2004.07.022.
32. S. Zhao, S. R. Froemming, S. Zhao, L. Gu, and S. R. Froemming, "Effects of Arterial Strain and Stress in the Prediction of Restenosis Risk: Computer Modeling of Stent Trials," Biomed. Eng. Lett., vol. 2, no. 3, pp. 158–163, 2012, doi: 10.1007/s13534-012-0067-6.
33. W. Wu, W.-Q. Wang, D.-Z. Yang, and M. Qi, "Stent expansion in curved vessel and their interactions: A finite element analysis," J. Biomech., vol. 40, no. 11, pp. 2580–2585, Jan. 2007, doi: 10.1016/j.jbiomech.2006.11.009.
34. I. Pericevic, C. Lally, D. Toner, and D. John, "The influence of plaque composition on underlying arterial wall stress during stent expansion : The case for lesion-specific stents," vol. 31, pp. 428–433, 2009, doi: 10.1016/j.medengphy.2008.11.005.
35. H. Zahedmanesh and C. Lally, "Determination of the influence of stent strut thickness using the finite element method: implications for vascular injury and in-stent restenosis," Med Biol Eng Comput. vol, vol. 47, no. 4, pp. 385–393, 2009.
36. A. Schiavone, L. G. Zhao, and A. A. Abdel-Wahab, "Dynamic simulation of stent deployment - effects of design, material and coating," J. Phys., vol. 451, no. 1, 2013, doi: 10.1088/1742-6596/451/1/012032.
37. A. Schiavone, L. G. Zhao, and A. A. Abdel-Wahab, "Effects of material, coating, design and plaque composition on stent deployment inside a stenotic artery—Finite element simulation," Mater. Sci. Eng. C, vol. 42, pp. 479–488, Sep. 2014, doi: 10.1016/j.msec.2014.05.057.
38. M. Imani, A. M. Goudarzi, D. D. Ganji, and A. L. Aghili, "The comprehensive finite element model for stenting: the influence of stent design on the outcome after coronary stent placement," J. Theor. app;ied Mech., vol. 51, no. 3, pp. 639–648, 2013.
39. A. Schiavone and L. GZhao, "A study of balloon type, system constraint and artery constitutive model used in finite element simulation of stent deployment," Mech. Adv. Mater. Mod. Process., 2015, doi: 10.1186/s40759-014-0002-x.
40. J. Xu, J. Yang, N. Huang, C. Uhl, Y. Zhou, and Y. Liu, "Mechanical response of cardiovascular stents under vascular dynamic bending," Biomed. Eng. Online, 2016, doi: 10.1186/s12938-016-0135-8.
41. A. Schiavone, T.-Y. Qiu, and L.-G. Zhao, "Crimping and deployment of metallic and polymeric stents - finite element modelling," Vessel Plus, 2017, doi: 10.20517/2574-1209.2016.03.
42. Ž. Donik, B. Nečemer, S. Glodež, and J. Kramberger, "Finite element analysis of the mechanical performance of a two-layer polymer composite stent structure," Eng. Fail. Anal., vol. 137, no. March, p. 106267, Jul. 2022, doi: 10.1016/j.engfailanal.2022.106267.
43. J. Bedoya, C. A. Meyer, L. H. Timmins, M. R. Moreno, and J. E. Moore, "Effects of stent design parameters on normal artery wall mechanics," J Biomech Eng, vol. 128, no. 5, pp. 757–765, 2006.
44. R. M. Hicks and P. A. Henne, "Wing Design by Numerical Optimization," J. Aircr., vol. 15, no. 7, pp. 407–412, Jul. 1978, doi: 10.2514/3.58379.
45. V. B. Kolachalama, N. W. Bressloff, P. B. Nair, and C. P. Shearman, "Predictive Haemodynamics in a One-Dimensional Human Carotid Artery Bifurcation. Part II: Application to Graft Design," IEEE Trans. Biomed. Eng., vol. 55, no. 3, pp. 1176–1184, Mar. 2008, doi: 10.1109/TBME.2007.912398.
46. M. Mooney, "A Theory of Large Elastic Deformation," J Appl Phys, vol. 11, no. 9, pp. 582–592, 1940, doi: 10.1063/1.1712836.
47. S. N. David Chua, B. J. Mac Donald, and M. S. J. Hashmi, "Finite element simulation of stent and balloon interaction," in Journal of Materials Processing Technology, 2003, vol. 143–144, no. 1, pp. 591–597, doi: 10.1016/S0924-0136(03)00435-7.
48. H. Zahedmanesh and D. John, "Simulation of a balloon expandable stent in a realistic coronary artery — Determination of the optimum modelling strategy," vol. 43, pp. 2126–2132, 2010, doi: 10.1016/j.jbiomech.2010.03.050.
49. A. Idziak-Jabłońska, K. Karczewska, and O. Kuberska, "Modeling of mechanical phenomena in the platinum-chromium coronary stents," J. Appl. Math. Comput. Mech., vol. 16, no. 4, pp. 29–36, 2017, doi: 10.17512/jamcm.2017.4.03.
50. D. S. S. Corp, "Dassault Systemes Abaqus 6.9.1 user manual."

2009.
51. D. Gastaldi, S. Morlacchi, R. Nichetti, C. Capelli, G. Dubini, and L. Petrini, "Modelling of the provisional side-branch stenting approach for the treatment of atherosclerotic coronary bifurcations: effects of stent positioning," Biomech. Model. Mechanobiol., vol. 9, no. 5, pp. 551–561, Oct. 2010, doi: 10.1007/s10237-010-0196-8.
52. L. Gu, S. Zhao, A. K. Muttyam, and J. M. Hammel, "The Relation Between the Arterial Stress and Restenosis Rate After Coronary Stenting," J. Med. Device., vol. 4, no. 3, p. 031005, Sep. 2010, doi: 10.1115/1.4002238.
53. F. Migliavacca, L. Petrini, V. Montanari, I. Quagliana, F. Auricchio, and G. Dubini, "A predictive study of the mechanical behaviour of coronary stents by computer modelling," Med. Eng. Phys., vol. 27, no. 1, pp. 13–18, Jan. 2005, doi: 10.1016/j.medengphy.2004.08.012.
54. G. A. Holzapfel, G. Sommer, C. T. Gasser, and P. Regitnig, "Determination of layer-specific mechanical properties of human coronary arteries with nonatherosclerotic intimal thickening and related constitutive modeling," Am. J. Physiol. Circ. Physiol., vol. 289, no. 5, pp. H2048–H2058, Nov. 2005, doi: 10.1152/ajpheart.00934.2004.
55. F. J. Gijsen, F. Migliavacca, S. Schievano, L. Socci, L. Petrini, and A. Thury, "Simulation of stent deployment in a realistic human coronary artery," Biomed. Eng. Online, vol. 7, no. 1, p. 23, 2008, doi: 10.1186/1475-925X-7-23.